

# Percolation and statistical properties of low- and high-angle interface networks in polycrystalline ensembles

Megan Frary and Christopher A. Schuh

*Department of Materials Science and Engineering, Massachusetts Institute of Technology, 77 Massachusetts Avenue, Cambridge, Massachusetts 02139, USA*

(Received 25 November 2003; revised manuscript received 20 January 2004; published 28 April 2004)

Percolation theory is often used to model intergranular or transgranular phenomena in polycrystals by treating low- and high-angle interfaces as strong and weak links, respectively. Here we demonstrate that triple-junction coordinations and percolation thresholds of such interfacial networks are significantly different from those of randomly assembled lattices, which invalidates the use of standard percolation theory for these problems. This departure is due to local crystallographic constraints for low- and high-angle boundary coordinations at triple junctions, which we understand here through (i) two-dimensional simulations of polycrystals with various textures and (ii) an analytical model using local transition probabilities. Both methods capture the tendency for high-angle boundaries to cluster, and the computational method also provides percolation threshold values for general and fiber-textured microstructures.

DOI: 10.1103/PhysRevB.69.134115

PACS number(s): 61.72.Mm, 64.60.Ak

## I. INTRODUCTION

Percolation theory is widely used to describe the structure and properties of polycrystalline materials, particularly for properties governed by interfaces that may be reasonably modeled as a network of “strong links” and “weak links” in the microstructure. Both intergranular and transgranular transport problems have been addressed in the framework of percolation theory and relate to nearly every field of condensed matter physics and materials science:

(i) Intergranular processes are those controlled by the transport of chemical species or defects (i.e., cracks) along the grain boundaries and include cracking,<sup>1–3</sup> corrosion,<sup>4–9</sup> electromigration,<sup>10,11</sup> dynamic embrittlement,<sup>12,13</sup> grain boundary wetting,<sup>14</sup> surface segregation,<sup>15</sup> and conductivity of dispersed ionic conductors.<sup>16</sup>

(ii) Transgranular phenomena are those in which a transport process occurs across the interfacial network, including conductivity,<sup>17,18</sup> superconductivity,<sup>19–23</sup> cleavage cracking,<sup>24–26</sup> and magnetoresistance.<sup>27</sup>

In the two-dimensional (2D) approximation, intergranular phenomena have been modeled with a standard bond percolation approach, while transgranular phenomena are modeled within the same framework using the concept of the dual lattice.<sup>28</sup> In nearly all probabilistic and percolation-based models of microstructures such as those cited above, the interfacial networks are modeled on a random basis, where bonds are assigned as strong or weak links, using only the fraction of each type as a microstructural state variable. The assumption that bonds are randomly assigned is fundamental to standard percolation theory, and it has only recently been appreciated that interfacial networks in polycrystalline ensembles cannot be described in this way due to intrinsic correlations imposed by crystallographic constraints. These constraints result in a network of grain boundaries that is distinctly different from a randomly assembled network by requiring that interfacial misorientations be conserved around any closed circuit through the microstructure. This condition imposes a constraint around any triple junction in the microstructure; for interfaces described by a misorienta-

tion matrix  $\mathbf{M}$ , the grain boundaries  $A$ ,  $B$ , and  $C$  that coordinate a triple junction must obey the crystallographic constraint

$$\mathbf{M}_A \mathbf{M}_B \mathbf{M}_C = \mathbf{I}, \quad (1)$$

where  $\mathbf{M}_X$  is the misorientation matrix of boundary  $X$  and  $\mathbf{I}$  is the identity matrix.<sup>29</sup>

In polycrystalline ensembles, the properties of interfaces are largely derived from their misorientations, so the classification of interfaces as “strong” or “weak” links is context dependent. For example, low-angle interfaces may be deemed favorable, and therefore any interface with a disorientation below a given threshold value will be labeled as a strong link, while all other interfaces are labeled as weak links. Other schemes may classify interfaces based on their ability to transmit dislocation slip between neighboring grains<sup>30–32</sup> or on their proximity to a coincidence site lattice (CSL) relationship.<sup>33–35</sup> In any of these cases, the constraint of Eq. (1) must hold, but the details of connectivity among strong- and weak-link interfaces will depend upon the classification scheme used. To date, the effect of crystallographic constraints on the percolation behavior of interfacial networks has only been appreciated for the case where interfaces are classified as CSL (strong link) or non-CSL (weak link). In this case, the deviations from standard percolation theory were first suggested by unexpected correlations among CSL and non-CSL boundaries at triple junctions (i.e., the triple-junction distribution) observed in experiments.<sup>36,37</sup> Subsequent Monte Carlo simulations of 2D microstructures incorporated crystallographic constraints for CSL boundaries and identified the percolation threshold for a continuous path of non-CSL boundaries to be  $p_c \sim 0.4–0.5$  (Ref. 38), greater than the threshold on a random lattice,  $p_c \approx 0.347$ .

Although the above works on networks of CSL grain boundaries have demonstrated the inadequacy of standard percolation theory for interfacial networks, the results cannot be easily generalized to other interfacial classification schemes. For example, the common division of grain boundaries into low- and high-angle varieties is known to correlate

with changes in their structure, energetics, and properties for virtually any material. With the exception of our recent preliminary report about percolation in tetragonal superconductors,<sup>39</sup> no works have identified the role of crystallographic constraints on the connectivity and percolation behavior of low- and high-angle grain boundary networks. The purpose of this paper is therefore to present a systematic exploration of these issues for cubic, hexagonal, and tetragonal polycrystals assembled in two-dimensional lattices. In Sec. II, we first present a survey of existing experimental data collected on many different materials of various symmetries, whose interfaces are classified as being either low or high angle. Extracting the experimental triple-junction distributions from these materials, we demonstrate that they are nonrandom and motivate the need for a crystallographically consistent theory of interfacial networks. In Sec. III, we present computer simulations that rationalize the experimental data and identify the percolation thresholds for interfacial networks. Finally, in Sec. IV, we develop a closed-form analytical solution for the triple-junction distribution in a crystallographically constrained fiber-textured polycrystal. Both the simulations and analytical model provide physical insight into how local constraints influence the global network topology.

## II. SURVEY OF EXPERIMENTAL GRAIN BOUNDARY NETWORKS

The triple-junction distribution<sup>37,38,40–43</sup> is a statistical description of the interfacial network connectivity and is given by the fraction of junctions  $J_i$ , which are coordinated by  $i$  ( $=0, 1, 2$ , or  $3$ ) low-angle boundaries. In a random assemblage of boundaries where each has the same probability  $p$  of being low angle, the complete triple-junction distribution is given by

$$J_0 = (1-p)^3, \quad (2a)$$

$$J_1 = 3p(1-p)^2, \quad (2b)$$

$$J_2 = 3p^2(1-p), \quad (2c)$$

$$J_3 = p^3. \quad (2d)$$

This distribution is shown by the lines in Fig. 1. To ascertain whether experimental microstructures follow this distribution, we have acquired the triple-junction distribution from experimental microstructures presented by other researchers studying low- and high-angle grain boundary networks.<sup>44–57</sup> The experimental data in Fig. 1 were taken from a wide variety of materials and crystal systems, including pure metals, intermetallic alloys, and superconducting oxides. Additionally, the definition of what constitutes a low-angle boundary varies among these studies, with the disorientation threshold  $\theta_l$  ranging from  $4^\circ$  to  $15^\circ$  as noted in the legend. Despite these differences, these independent data sets all lie on reasonably common trend lines in Fig. 1. Furthermore, the collected data clearly do not follow the expected random distribution, showing a significant reduction of  $J_2$  junctions and a concurrent increase in  $J_3$  junctions. These deviations

Symbol	Material	Space Group	$\theta_l$ (deg)	Reference
○	Nickel	Fm $\bar{3}m$	15	44
▲	Nickel	Fm $\bar{3}m$	15	45
△	Nickel	Fm $\bar{3}m$	15	52
●	Nickel	Fm $\bar{3}m$	4	50
⊠	Nickel	Fm $\bar{3}m$	10	54
⊞	Nickel	Fm $\bar{3}m$	7	50
▴	Nickel	Fm $\bar{3}m$	5	56
◆	Nickel	Fm $\bar{3}m$	10	56
◇	8090 Al-Li alloy	Fm $\bar{3}m$	15	46
□	Aluminum 5052	Fm $\bar{3}m$	15	51
□	Cu-1Al	Fm $\bar{3}m$	15	49
⊞	Platinum	Fm $\bar{3}m$		57
▽	Fe-35Al-4.3Cr-0.1Zr-0.05B	Pm $\bar{3}m$	15	48
■	(Bi,Pb) <sub>2</sub> Sr <sub>2</sub> Ca <sub>2</sub> Cu <sub>3</sub> O <sub>x</sub>	14/mmm	15	47
▲	(Bi,Pb) <sub>2</sub> Sr <sub>2</sub> Ca <sub>2</sub> Cu <sub>3</sub> O <sub>x</sub>	14/mmm	15	53
▼	YBa <sub>2</sub> Cu <sub>3</sub> O <sub>7</sub>	Pmmm	10	55

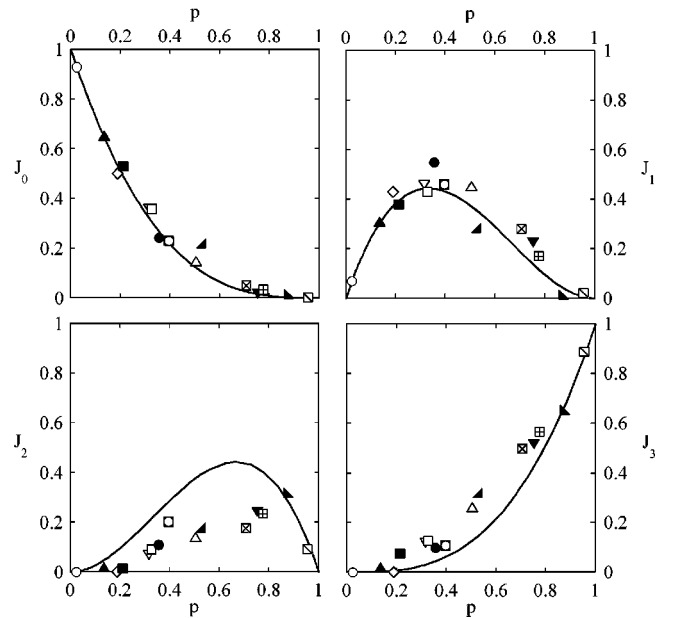


FIG. 1. Triple-junction distributions from existing experimental data (points), covering a range of materials and crystal systems, including pure metals, intermetallic alloys, and superconducting oxides, with low-angle thresholds  $\theta_l$  between  $4^\circ$  and  $15^\circ$ . These data are compared to the triple-junction distribution for a random assemblage of boundaries as given by Eq. (2) (solid lines).

have never been explicitly noted before for the case of low- and high-angle interfaces, and are symptomatic of an underlying topological constraint which affects the local interfacial connectivity. These data underscore the fact that standard percolation models cannot be applied to networks of low- and high-angle interfaces; instead, new crystallographically consistent models are required, as discussed below.

## III. COMPUTATIONAL MODEL

### A. Simulation procedures

To study the network topology and percolation behavior of low- and high-angle grain boundaries in polycrystalline

ensembles, we construct two-dimensional lattices in which each grain has six nearest neighbors and all nodes of the interfacial network are triple junctions. The crystal structure of the grains was taken to be either cubic, hexagonal, or tetragonal, and one of two different methods was used to assign orientations to each grain:

(i) In the first method, all grains were initially assigned the same orientation and then individually rotated randomly within a prescribed tolerance  $\phi_{\max}$  about a common, high-symmetry axis. The resulting microstructures resemble perfect fiber textures and can be compared with, e.g., epitaxial films or extruded materials. As will be seen later, this simplified microstructure also admits an analytical solution for the triple-junction distribution.

(ii) In the second method, each grain was assigned an orientation within a prescribed tolerance  $\phi_{\max}$  of a reference orientation, in such a manner as to give uniform coverage of orientation space within the region prescribed by  $\phi_{\max}$ . This procedure creates a single, unspecified texture component in the structure (e.g., a “cube texture” in cubic lattices). Since many textures can be described as superpositions of just a few select components, this case allows ready extension to many practical situations and is also expected to compare with the experimental data assembled above.

In the discussion to follow, we refer to the above cases as “fiber texture” and “general texture,” respectively. For both cases, the strength of the texture was controlled through the choice of  $\phi_{\max}$ , with smaller values promoting sharper textures. Grain boundary disorientations  $\theta$  were found for each grain boundary in the interfacial network from the known orientations of adjacent grains<sup>58</sup> and then classified as either low or high angle for disorientations, respectively, below or above a given threshold  $\theta_t$ . For most of what follows, we have used the typical value  $\theta_t = 15^\circ$ , although other values from  $2^\circ$  to  $10^\circ$  have also been considered in some computations. Once the binary characterization of boundaries was complete, a standard Hoshen-Kopelman algorithm was used to identify and track grain boundary clusters.<sup>59</sup> Several hundred lattices were constructed, and the percolation threshold was taken to be the low-angle fraction where half of the lattices contained a percolating cluster. By increasing the size of the lattice to 1000 grains per side, this approach allowed the percolation threshold to be determined with an accuracy of  $\pm 0.005$ .

### B. Characterization of simulated structures

The two-dimensional microstructures produced by the above procedures are characterized principally by the one-point statistical distribution of grain orientations, as illustrated in standard pole figures. The control parameter  $\phi_{\max}$  directly dictates the sharpness of the texture as shown in Fig. 2, where typical discrete (100) pole figures are given for simulated fiber-textured tetragonal polycrystals with various values of  $\phi_{\max}$ . At high values of  $\phi_{\max}$ , a typical fiber texture exists in the material [Fig. 2(a)], and lower values of  $\phi_{\max}$  promote a sharpening of the texture [Figs. 2(b) and 2(c)], until there is almost no misalignment between grains [Fig. 2(d)].

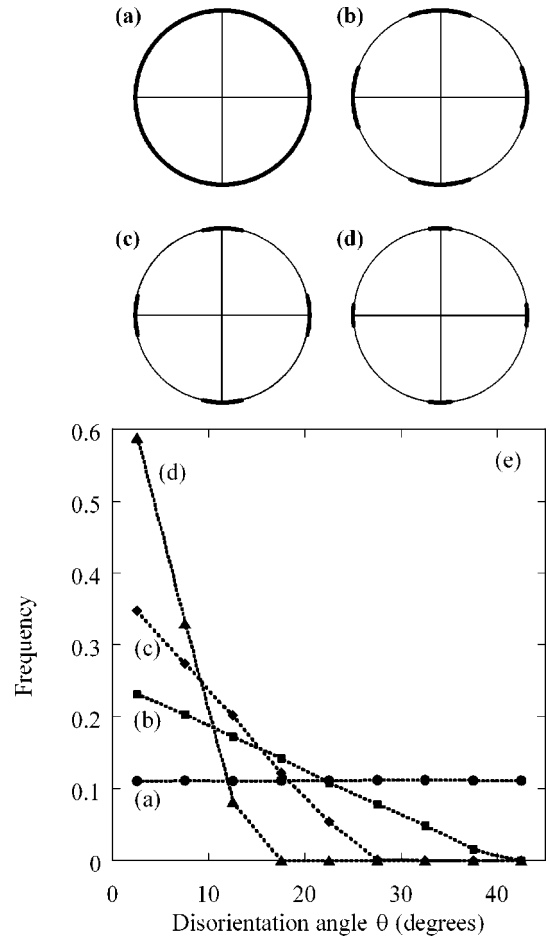


FIG. 2. (100) pole figures for fiber-textured tetragonal polycrystals with  $\phi_{\max} = 45^\circ$  (a),  $20^\circ$  (b),  $13^\circ$  (c), or  $7^\circ$  (d). The disorientation angle distributions that correspond to each texture are given in (e).

The evolution of the texture as described above also influences the two-point misorientation distribution of the simulated polycrystals, as shown by the grain boundary disorientation angle distributions in Fig. 2(e). When  $\phi_{\max}$  is small [Fig. 2(d)], nearly all of the boundaries have disorientations less than  $15^\circ$ . As  $\phi_{\max}$  increases, the fraction of boundaries with low disorientation angles decreases, corresponding to a weakening of the texture. In these fiber-textured microstructures, where grain rotation occurs around a common axis, the maximum disorientation between grains,  $\Theta_M$ , is given by the symmetry of that axis; e.g., there are  $\pm 30^\circ$  of unique orientation for rotation about the  $c$  axis in hexagonal polycrystals and  $\pm 45^\circ$  in cubic or tetragonal polycrystals. If the rotational tolerance  $\phi_{\max}$  is less than half of  $\Theta_M$ , the disorientation distribution is essentially a sloped line that intersects the horizontal axis at  $2\phi_{\max}$ . When  $2\phi_{\max}$  exceeds  $\Theta_M$ , the disorientation distribution begins to level off, such that for very high  $\phi_{\max}$ , the distribution is uniform.

The simulated microstructures with general textures are also characterized by the same statistical distributions. In Fig. 3, typical discrete (001) pole figures are given for simulated cubic polycrystals with various values of  $\phi_{\max}$ . At high values of  $\phi_{\max}$  [Fig. 3(a)], a nearly random texture exists in

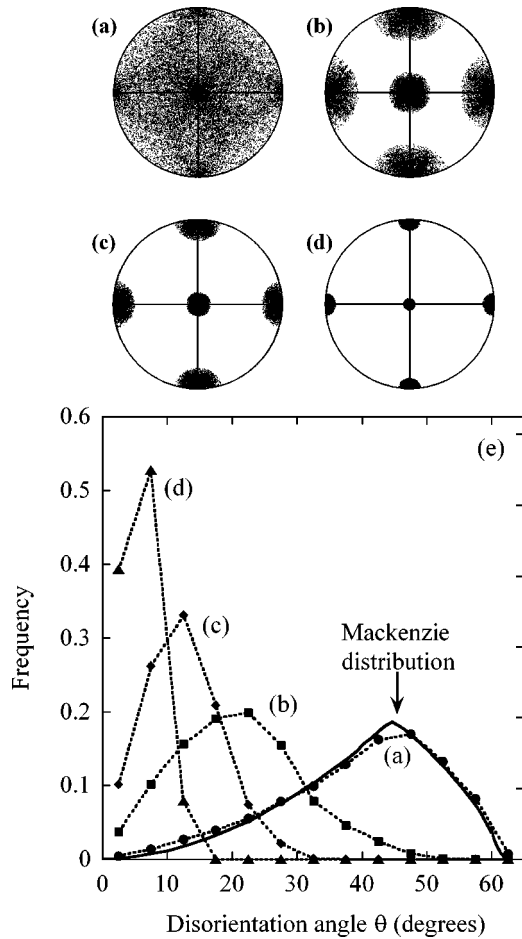


FIG. 3. (001) pole figures for general texture in cubic polycrystals with  $\phi_{\max}=95^\circ$  (a),  $28^\circ$  (b),  $16.5^\circ$  (c), or  $7^\circ$  (d). The disorientation angle distributions that correspond to each texture are given in (e), along with the Mackenzie distribution for randomly oriented cubic polycrystals (Ref. 60).

the material, and as before, lower values of  $\phi_{\max}$  sharpen the texture [Figs. 3(b) and 3(c)] until a strong cube texture results for very low  $\phi_{\max}$  [Fig. 3(d)]. The evolution of the general textured microstructures may also be seen through the disorientation angle distributions in Fig. 3(e). Unlike the case of a fiber texture where high values of  $\phi_{\max}$  resulted in a uniform distribution, here an increase in  $\phi_{\max}$  shifts the distribution toward the Mackenzie distribution for randomly oriented cubic polycrystals.<sup>60</sup> A similar evolution of the texture and disorientation distribution in polycrystals with hexagonal symmetry can be seen in Fig. 4. Here the  $(10\bar{1}0)$  pole figures show a single texture component that sharpens with decreasing  $\phi_{\max}$  and the concomitant shift of the disorientation angle distribution toward that of randomly oriented hexagonal polycrystals.<sup>61</sup>

The relationship between the texture and grain boundary character is summarized in Fig. 5. Here the sharpness of the texture is given by the rotational tolerance  $\phi_{\max}$ . Similarly, the misorientation distribution has also been collapsed into a single parameter  $p$ , the fraction of low-angle boundaries. As shown in Fig. 5 for tetragonal, hexagonal, and cubic polycrystals with low-angle threshold  $\theta_l=15^\circ$ , all of the crystal

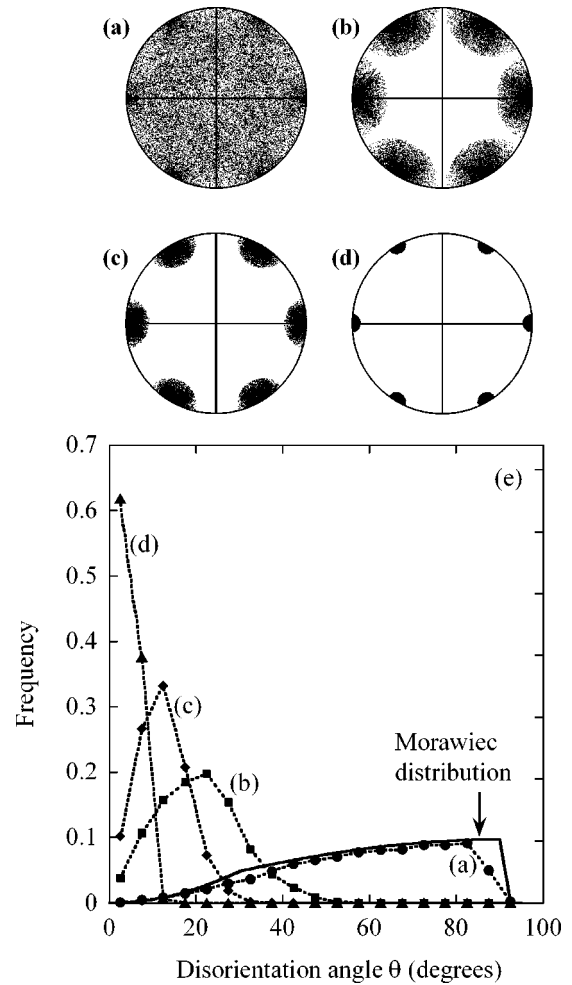


FIG. 4.  $(10\bar{1}0)$  pole figures for general texture in hexagonal polycrystals with  $\phi_{\max}=95^\circ$  (a),  $28^\circ$  (b),  $16.5^\circ$  (c), or  $7^\circ$  (d). The disorientation angle distributions that correspond to each texture are given in (e), along with the Morawiec distribution for randomly oriented hexagonal polycrystals (Ref. 61).

systems show similar behavior, with a minimum grain rotation of  $7.5^\circ$  required before there are any high-angle boundaries in the microstructure. Although the form of the curves in Fig. 5 changes with the definition of a low-angle boundary (i.e., with choice of  $\theta_l$ ), the important point illustrated here is that there is a well-defined and monotonic relationship between the texture of the simulated polycrystals and their low-angle boundary fraction. This intuitive result has been reached by several prior investigators using similar simulations<sup>51,62–64</sup> and has an important implication for the study of network topology to follow. Specifically, percolation theory is framed explicitly in terms of the fraction  $p$  as well as its complement,  $q \equiv 1 - p$ . Because  $p$  is simply related to the texture as in Fig. 5,  $p$  can be regarded, for the purposes of discussion, as the “control parameter” with respect to the topology of the resulting grain boundary network. Therefore, in what follows,  $p$  is used as the principal descriptor of our simulated interfacial networks, and it should be remembered that  $p$  is monotonically related to the sharpness of texture. Our simulations and analytical developments that follow will

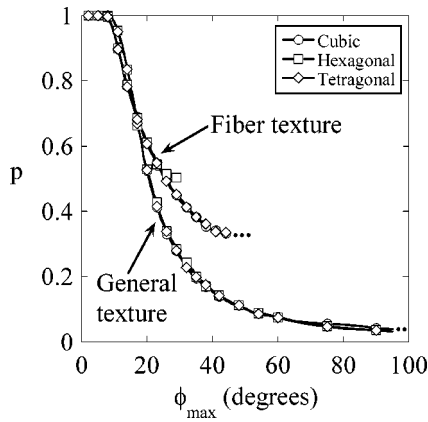


FIG. 5. Low-angle fraction  $p$  as a function of the sharpness of texture, given by the rotational tolerance  $\phi_{\max}$ , for polycrystals with cubic, hexagonal, and tetragonal symmetry where the low-angle threshold is  $15^\circ$ . For the fiber-textured microstructures, the curves are truncated at the minimum value of  $p$  achievable as explained in the text.

also be shown to validate the use of  $p$  as a microstructural state variable.

### C. Topology of simulated interfacial networks

As described in the Introduction, the topology of a realistic interfacial network can differ greatly from that of a ran-

dom network. To illustrate this point, we have constructed networks of interfaces using the typical approach of percolation theory, whereby each interface is assigned as low angle or high angle with probability  $p$  or  $q$ , respectively, without regard for crystallography. The constraining effects of crystallography can then be appreciated qualitatively by direct observation of the spatial distribution of high-angle boundaries on two-dimensional lattices. In Fig. 6, the high-angle boundaries are highlighted on small hexagonal lattices with  $p=0.5$  and  $0.7$  for grain boundary networks that were assembled both randomly and using the crystallographically consistent methods described earlier. In the randomly assembled lattices [Figs. 6(a) and 6(d)], the spatial distribution of high-angle boundaries is expectedly uniform, with no obvious tendency to cluster beyond that which occurs by chance. In contrast, the high-angle boundaries in the crystallographically constrained networks tend to cluster together, especially in the form of long strings [Fig. 6(b)] or small, complete rings [Fig. 6(c)]. In these lattices, whether they are for the fiber or general texture (i.e., with or without a shared crystallographic axis), there are large regions in which only low-angle boundaries exist; enforcing consistent crystallography results in a patchier grain boundary network.

The clustering tendency observed above may be quantified by considering the triple-junction distributions, which are given in Fig. 7 for the crystallographically consistent lattices with both fiber and general textures. These curves

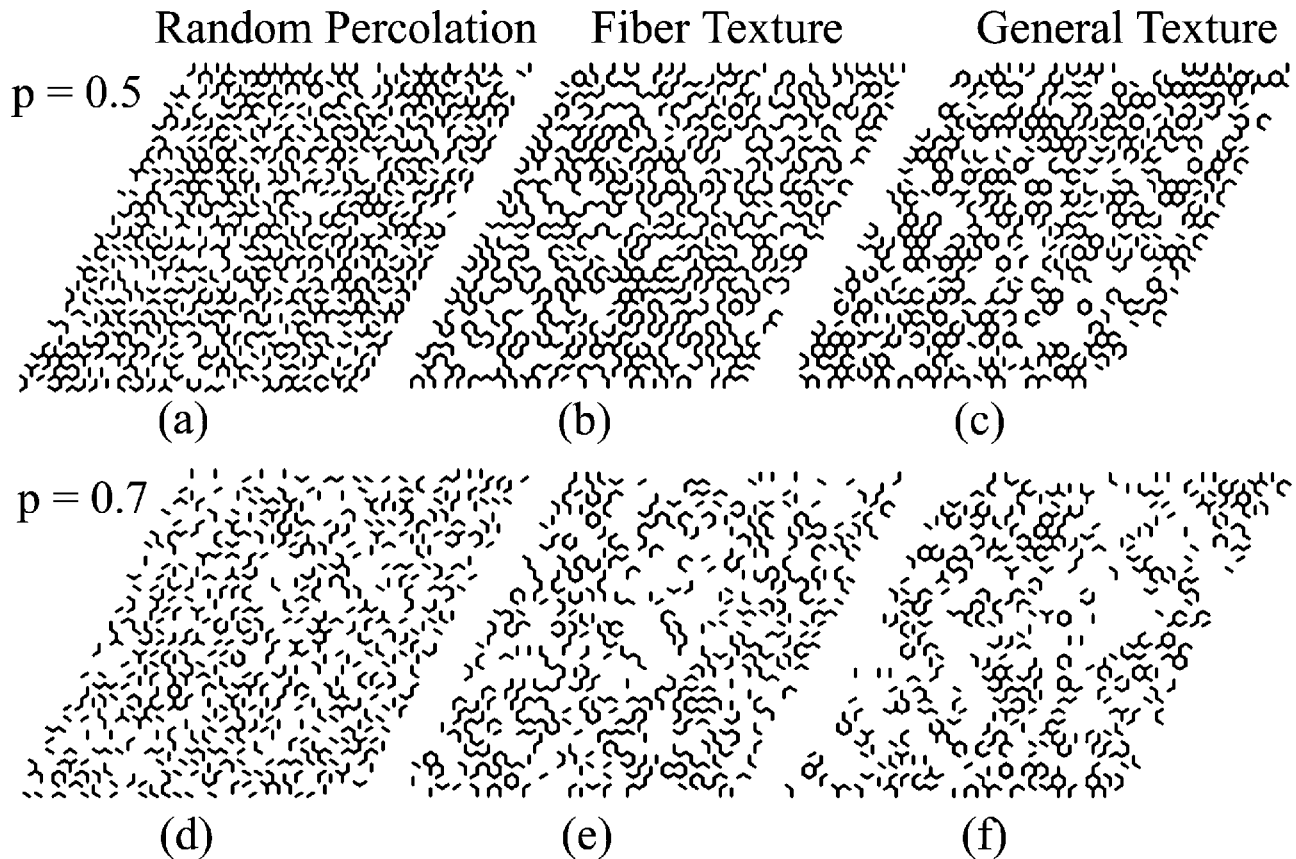


FIG. 6. Spatial distribution of high-angle boundaries for  $p=0.5$  (top row) and  $0.7$  (bottom row) on small, two-dimensional hexagonal lattices that were assembled randomly (a), (d) or with crystallographic consistency [(b), (e) fiber texture, (c), (f) general texture].

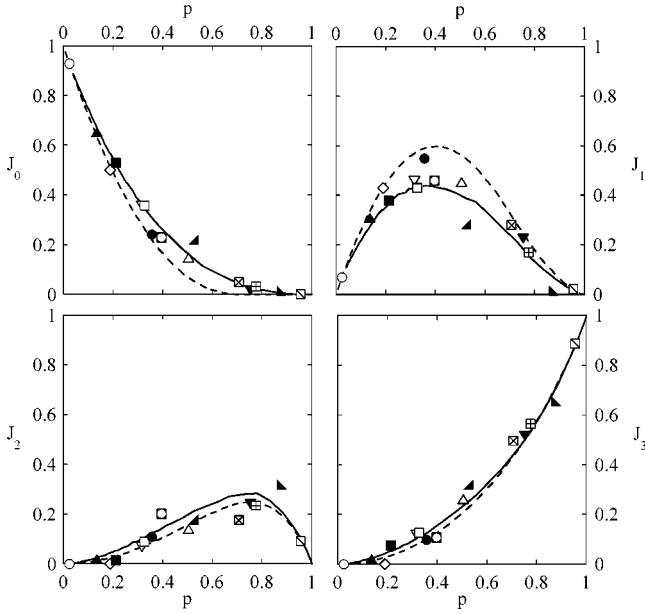


FIG. 7. Triple-junction distribution for simulated microstructures with crystallographic consistency (fiber texture, dashed lines; general texture, solid lines). Also shown are the experimental triple-junction distributions, where the symbols are the same as in Fig. 1.

should be compared with those in Fig. 1 for the random case. The population of  $J_2$  junctions (two low-angle boundaries) in both types of constrained lattices is considerably diminished with respect to the random lattices, while there is a relative increase in the population of  $J_3$  junctions. In the fiber-textured microstructures, there is a significant increase in the fraction of  $J_1$  junctions as well. These results quantitatively capture the clustering observed in Figs. 6(b), 6(c), 6(e), and 6(f) where there are few junctions coordinated by only one high-angle boundary ( $J_2$  junctions, which appear as “dangling bonds” in Fig. 6).

An important point that is not explicitly observed in Fig. 7 is that the triple-junction distributions have been determined for lattices with cubic, hexagonal, and tetragonal symmetry, and we find that crystal symmetry has *no measurable effect* on this distribution among the centrosymmetric crystal systems. Furthermore, the triple-junction distributions in Fig. 7 are also found to be independent of the low-angle boundary threshold  $\theta_l$ . Changes in  $\theta_l$  affect the sharpness of texture required to produce a given low-angle fraction  $p$ , but do not change the network topology in a fundamental way. This result supports the use of  $p$  as a state variable. Furthermore, the invariance of the triple-junction distribution with changes in  $\theta_l$  or even crystal symmetry suggests that the curves in Fig. 7 can be regarded essentially as universal expectation curves for any polycrystal. This explains why many independent experiments lie on common curves in Fig. 7, and in fact the simulation results match quite closely with the collected data. Although these simulations have modeled a single-component texture, very similar triple-junction distributions can also be expected for multicomponent textures which, in the present context, would be superpositions of these single-texture component results. However, in a homogeneous microstructure with  $T$  distinct texture components, the maxi-

TABLE I. Percolation thresholds for a continuous path of low-angle ( $p_{c,\text{LAB}}$ ) or high-angle ( $p_{c,\text{HAB}}$ ) boundaries for both fiber and general textured microstructures, as determined on lattices with 1000 grains per side. Variation in crystal symmetry (cubic, hexagonal, or tetragonal) and low-angle threshold ( $\theta_l = 2^\circ - 15^\circ$ ) has no effect on the percolation threshold.

	$\theta_l$ (deg)	$p_{c,\text{LAB}} (\pm 0.005)$	$p_{c,\text{HAB}} (\pm 0.005)$
Random lattice		0.653	0.347
General texture			
Cubic	15	0.664	0.324
Hexagonal	15	0.664	0.324
Tetragonal	15	0.663	0.324
Fiber texture			
Cubic	15	0.687	0.399
Hexagonal	15	0.687	<sup>a</sup>
Tetragonal	15	0.687	0.399
Tetragonal	10	0.687	0.399
Tetragonal	8	0.686	0.399
Tetragonal	6	0.687	0.400
Tetragonal	4	0.687	0.400
Tetragonal	2	0.687	0.399

<sup>a</sup>The minimum low-angle fraction that can be achieved is 50%, given by the symmetry of the structure and the low-angle threshold, such that there will never be a continuous path of high-angle boundaries.

imum achievable low-angle fraction is  $\sim 1/T$ , since texture components are usually separated by more than  $\theta_l = 15^\circ$  of rotation.

The deviation of the triple-junction distributions in Fig. 7 from the random populations in Fig. 1 is due to the crystallographic consistency required by Eq. (1). Using the crystallographic constraint of Eq. (1), we have recently derived the relationship that governs the disorientations of grain boundaries at a triple junction as<sup>65</sup>

$$\theta_{\text{max}} \leq \theta_1 + \theta_2, \quad (3)$$

where  $\theta_{\text{max}}$  is the maximum disorientation of the three boundaries at the junction and  $\theta_1$  and  $\theta_2$  are the other two disorientations. Accordingly, if two of the boundaries (e.g.,  $\theta_1$  and  $\theta_2$ ) have low disorientation angles, it is unlikely that their sum will exceed the low-angle boundary threshold, resulting in relatively few junctions coordinated by two low-angle boundaries.

#### D. Percolation thresholds

The percolation thresholds we have identified for 2D polycrystals with various textures, crystal symmetries, and low-angle thresholds are summarized in Table I. Here we have tabulated the percolation threshold for a continuous path of low-angle boundaries, called  $p_{c,\text{LAB}}$ , as well as the complementary threshold at which there is no longer a continuous path of high-angle boundaries,  $p_{c,\text{HAB}}$ . As we found above with respect to the triple-junction distributions, there is no effect of crystal structure or  $\theta_l$  on either percolation

threshold within the accuracy of this study (Table I). Furthermore, all of the values of  $p_c$  identified here for polycrystals are distinctly different from those observed in random lattices. For example, values of  $p_{c,\text{LAB}} \approx 0.687$  and  $p_{c,\text{HAB}} \approx 0.399$  were found for fiber textures, which are different from the respective values 0.653 and 0.347 in the random case. It is also interesting to note that the enforcement of crystallographic constraint breaks the symmetry normally seen in percolation problems; whereas  $p_{c,\text{LAB}} = 1 - p_{c,\text{HAB}}$  for a random lattice, this is not generally true in polycrystals.

The deviations of  $p_c$  in Table I from the random cases are consistent with the triple-junction distribution in Fig. 7 and also can be rationalized qualitatively by examination of the networks in Fig. 6. For example, for polycrystals with a fiber texture we find  $p_{c,\text{HAB}} = 0.399 \pm 0.005$ , higher than that of a random lattice at 0.347. At the same time, the network of high-angle grain boundaries in Fig. 6(e) has a considerably stringier structure than does the random network in Fig. 6(d), with longer chains of high-angle boundaries and fewer grains surrounded by high-angle boundaries. This change in topology corresponds to a significant increase in  $J_1$  junctions above the random value (Fig. 7), and the tendency of high-angle boundaries to assemble into long chains slightly reduces the population needed for a spanning cluster. In the case of general texture,  $p_{c,\text{HAB}} \approx 0.324$  is somewhat lower than the random value of 0.347, which is a result of a tendency to form large clusters rather than strings. In Fig. 6(f), it is clear that both the low- and high-angle boundaries tend to cluster with like boundaries, corresponding to an increase in  $J_0$  and  $J_3$  junctions over the random distributions and a suppression of  $J_1$  and  $J_2$  junctions.

With regard to the percolation thresholds for low-angle boundaries, both fiber and general textures exhibit a threshold  $p_{c,\text{LAB}} \approx 0.67\text{--}0.69$ , higher than the expected value of  $p_{c,\text{LAB}} = 0.653$  for a randomly assembled lattice. This result implies that a relative excess of low-angle boundaries is needed for a continuous path to develop and results from the scarcity of  $J_2$  junctions seen in these structures [Figs. 6(e) and 6(f)]. Since the  $J_2$  junctions most facilitate the connectivity of low-angle boundaries across the lattice, crystallographic suppression of these junctions requires  $p_{c,\text{LAB}}$  to increase.

#### IV. ANALYTICAL MODEL

In Secs. II and III, we have shown through a survey of experimental grain boundary networks and computer simulations that the percolation behavior and local triple-junction distributions of polycrystals are nonrandom. There currently exist no closed-form analytical solutions for these nonrandom distributions, however. In what follows, we will develop such a solution in the case of fiber-textured microstructures, where the grain boundary disorientations have a rigid constraint. Our analytical results will also offer physical insight into the role of crystallographic constraints on the topology of interfacial networks.

##### A. Analytical approach

The triple-junction distribution  $J_i$ , as described in Sec. II C, gives the fraction of junctions coordinated by  $i$  low-

angle boundaries. If all boundaries have a probability  $p$  of being assigned as low-angle boundaries, then the triple-junction distribution is given by Eq. (2). However, as we will show explicitly in what follows, around triple junctions that obey the constraint of Eq. (1), the probabilities for each boundary assignment are not independent, and these local probabilities depend not only on how many of the three boundaries have been assigned, but on their character as well. For example, the first grain boundary at any triple junction can be assigned a misorientation on a truly random basis with a probability  $p$  of being assigned as a low-angle boundary. Once the first boundary at the triple junction has been assigned, however, there exists a limited range of misorientations that the second boundary may take on, such that its being assigned as a low-angle boundary is dependent on the disorientation of the first boundary. Furthermore, once the first two boundaries have been assigned, the disorientation of the third boundary is fixed by the crystallographic constraint [Eq. (1)]. In order to find the triple-junction distribution in a crystallographically consistent lattice, we seek expressions for these local transition probabilities, defined as  $\Pi_x^y$ , the density distribution of low-angle boundaries at a triple junction where  $y$  ( $=0, 1$ , or  $2$ ) boundaries have been assigned,  $x$  ( $\leq y$ ) of which have been classified as low-angle boundaries. In terms of these probabilities  $\Pi_x^y$ , which are order dependent, the triple-junction distribution is given as

$$J_0 = (1 - \Pi_0^0)(1 - \Pi_0^1)(1 - \Pi_0^2), \quad (4a)$$

$$J_1 = \Pi_0^0(1 - \Pi_1^1)(1 - \Pi_1^2) + (1 - \Pi_0^0)\Pi_0^1(1 - \Pi_1^2) + (1 - \Pi_0^0)(1 - \Pi_0^1)\Pi_0^2, \quad (4b)$$

$$J_2 = \Pi_0^0\Pi_1^1(1 - \Pi_2^2) + \Pi_0^0(1 - \Pi_1^1)\Pi_1^2 + (1 - \Pi_0^0)\Pi_0^1\Pi_1^2, \quad (4c)$$

$$J_3 = \Pi_0^0\Pi_1^1\Pi_2^2. \quad (4d)$$

The expressions for  $J_1$  and  $J_2$  each have three terms, as there are three possible configurations for each junction type (e.g., the single low-angle boundary in a  $J_1$  junction could be associated with either the first, second, or third boundary). In the unconstrained system when all boundaries are assigned randomly, there is no order dependence as to whether any given boundary will be assigned as low angle—i.e., all  $\Pi_x^y = p$ —and Eq. (4) reduces to the form of the random triple-junction distribution of Eq. (2). We note that Eq. (4) represents a generalization of the method used by Minich *et al.* in their study of triple junctions in CSL networks.<sup>42</sup> Those authors assumed that the first two boundaries at a triple junction could be assigned a character at random and introduced local transition probabilities for the assignment of the third boundary ( $\Pi_x^2$ ). As we will demonstrate presently for the case of low- and high-angle boundaries, all six terms ( $\Pi_x^y$ ) are required and can be obtained in closed form.

##### B. Relationship among the global variables

To simplify the analytical treatment, we confine our attention to the case of the ideal fiber-textured material, such that

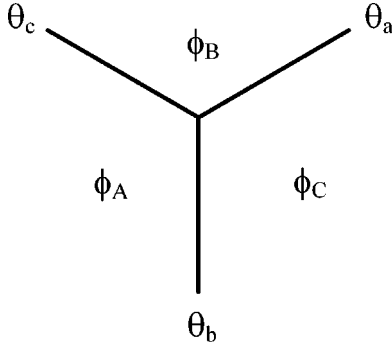


FIG. 8. Labeling scheme for angles at a triple junction;  $\phi_X$  are grain orientations which occupy the range  $(-\phi_{\max}, \phi_{\max})$ , while  $\theta_x$  are grain boundary disorientations and exist on the range  $(-2\phi_{\max}, 2\phi_{\max})$ .

the state of each grain is fully specified by a single in-plane orientation angle. The geometry and nomenclature of the system is shown schematically in Fig. 8. The orientations of the three grains A, B, and C that meet at the triple junction are labeled  $\phi_A$ ,  $\phi_B$ , and  $\phi_C$ , and may assume any value on the range  $(-\phi_{\max}, \phi_{\max})$ . These angles represent in-plane rotations about a line parallel to the triple-junction axis. The grain boundary disorientation angles are  $\theta_a$ ,  $\theta_b$ , and  $\theta_c$ , where, as a convention, boundary *a* is taken to be opposite grain A (Fig. 8). Although disorientation angles are typically unsigned, the derivation to follow is simplified by allowing both positive and negative disorientations. Then, because all grains share a common axis, the grain boundary disorientations may be found as the difference between the orientations of neighboring grains, e.g.,

$$\theta_c = \phi_A - \phi_B, \quad (5)$$

and may take any value on the range  $(-2\phi_{\max}, 2\phi_{\max})$ . The angle  $\phi_{\max}$ , as before, controls the sharpness of the texture and also the range of grain boundary disorientation angles in the interfacial network. The grain boundary disorientations are defined around a clockwise circuit and therefore are constrained by the relationship

$$\theta_a + \theta_b + \theta_c = 0. \quad (6)$$

In Sec. III C, the crystallographic constraint was given by the inequality of Eq. (3); when the grains share a common rotation axis, the equation simplifies to an equality, and Eq. (6) is simply Eq. (3) when the interface disorientations may take both positive and negative values.

The distribution of grain boundary disorientations may now be obtained through convolution of the grain orientation distributions as

$$F(\theta_c) = \int_{-\infty}^{\infty} F(\phi_A)F(\phi_B)d\phi_B, \quad (7)$$

where  $F(\alpha)$  is the global density distribution of either an orientation or disorientation angle  $\alpha$ . Since grain orientations are assigned at random,  $F(\phi)$  is a uniform distribution:

$$F(\phi) = \begin{cases} \frac{1}{2\phi_{\max}}, & -\phi_{\max} \leq \phi \leq \phi_{\max}, \\ 0, & \text{otherwise,} \end{cases} \quad (8)$$

where the subscript on  $\phi$  has been omitted, since Eq. (8) applies to all three grains A, B, and C. If we substitute for  $\phi_A$  according to Eq. (5) such that  $\phi_B$  is the only remaining variable, Eq. (7) becomes

$$F(\theta_c) = \int_{-\infty}^{\infty} F(\theta_c + \phi_B)F(\phi_B)d\phi_B. \quad (9)$$

Introducing Eq. (8) and integrating now yields the global density distribution of boundary disorientations:

$$F(\theta) = \begin{cases} \frac{1}{4\phi_{\max}^2}(2\phi_{\max} + \theta), & -2\phi_{\max} \leq \theta \leq 0, \\ \frac{1}{4\phi_{\max}^2}(2\phi_{\max} - \theta), & 0 \leq \theta \leq 2\phi_{\max}, \\ 0, & \text{otherwise.} \end{cases} \quad (10)$$

Again, no subscript is given for  $\theta$ , since this result applies for any of the boundaries at the triple junction. If an angular threshold  $\theta_t$  is then applied below which boundaries are classified as low angle, the global low-angle boundary fraction  $p$  can be found as the fraction of boundaries in the global distribution with absolute disorientations less than  $\theta_t$ :

$$p = \frac{\int_{-\theta_t}^{\theta_t} F(\theta)d\theta}{\int_{-\infty}^{\infty} F(\theta)d\theta}. \quad (11)$$

If Eq. (11) is applied to the density distribution in Eq. (10), the resulting global low-angle fraction is obtained in terms of  $\theta_t$  and  $\phi_{\max}$ :

$$p = \frac{\theta_t}{\phi_{\max}} - \left(\frac{\theta_t}{2\phi_{\max}}\right)^2. \quad (12)$$

It is now evident from Eq. (12) how, for a given low-angle threshold  $\theta_t$ , the value of the low-angle fraction may be adjusted by redefining the orientation tolerance  $\phi_{\max}$ . The simulated interfacial networks described earlier match exactly the global distributions described above as well as the trend of Eq. (12) (cf. Fig. 5).

### C. Local transition probabilities

It is important to note that Eqs. (10) and (12) define the *global* disorientation density distribution and low-angle boundary fraction, properties that are averaged over a large ensemble. Therefore, within the same framework used above, we now develop analytical expressions for the local density distribution functions  $\Pi_x^y$  by considering the role of the crystallographic constraint on the distributions  $F(\theta)$  at individual triple junctions. Our procedure will be as follows. Starting with the generic triple junction in Fig. 8, we first assign two of the three degrees of freedom of the system by making a choice as to the disorientation of boundary *a*. We then derive the effect that this has on the subsequent choice

of a second disorientation  $\theta_b$  by determining the density distribution function  $f(\theta_b)$  at a given value of  $\theta_a$ , from which the global distribution  $F(\theta_b)$  may subsequently be obtained. When these two misorientations are chosen, the third,  $\theta_c$ , is given explicitly by Eq. (6).

To begin, we assume a unique and known value for  $\theta_a$ , fixing the relationship between  $\phi_B$  and  $\phi_C$ . Then, the range of allowed values for  $\phi_C$  (bounded by  $\phi_{C,\min}$  and  $\phi_{C,\max}$ ) may be found from Eq. (5) by noting that  $\phi_B$  exists on the range  $(-\phi_{\max}, \phi_{\max})$ :

$$\phi_{C,\max} = \begin{cases} \phi_{\max}, & \theta_a \leq 0, \\ \phi_{\max} - \theta_a, & \theta_a > 0, \end{cases} \quad (13a)$$

$$\phi_{C,\min} = \begin{cases} -\phi_{\max} - \theta_a, & \theta_a \leq 0, \\ -\phi_{\max}, & \theta_a > 0. \end{cases} \quad (13b)$$

Equation (13) indicates that the random assignment of one disorientation  $\theta_a$  already places a restriction upon the remaining degree of freedom in the system; instead of being randomly distributed on the range  $(-\phi_{\max}, \phi_{\max})$ ,  $\phi_C$  distributes only over the ranges given in Eq. (13). We now seek the density distribution of  $\theta_b$  for a known value of  $\theta_a$ , which is denoted as  $f(\theta_b)$  to distinguish it from the global density distribution  $F(\theta_b)$ . The function  $f(\theta_b)$  is defined implicitly by the fact that when integrated over all acceptable values of  $\theta_a$ , it yields  $F(\theta_b)$ :

$$F(\theta_b) = \int_{-\infty}^{\infty} f(\theta_b) d\theta_a. \quad (14)$$

The distribution  $f(\theta_b)$  can be found through the convolution of  $F(\phi_A)$  with  $F(\phi_C)$ , which is a uniform random distribution on the range given in Eq. (13):

$$f(\theta_b) = \frac{F(\theta_a)}{2\phi_n} \int_{-\phi_{\max}}^{\phi_{\max}} F(\theta_b + \phi_A) d\phi_A, \quad (15)$$

which is readily soluble; when  $\theta_a < 0$ ,

$$f(\theta_b) = \frac{1}{2\phi_{\max}} \begin{cases} 0, & -2\phi_{\max} < \theta_b < -2\phi_{\max} - \theta_a, \\ 2\phi_{\max} + \theta_a + \theta_b, & -2\phi_{\max} - \theta_a < \theta_b < 0, \\ 2\phi_{\max} + \theta_a, & 0 < \theta_b < -\theta_a, \\ 2\phi_{\max} - \theta_b, & -\theta_a < \theta_b < 2\phi_{\max}, \end{cases} \quad (16a)$$

and when  $\theta_a > 0$ ,

$$f(\theta_b) = \frac{1}{2\phi_{\max}} \begin{cases} 2\phi_{\max} + \theta_b, & -2\phi_{\max} < \theta_b < -\theta_a, \\ 2\phi_{\max} - \theta_a, & -\theta_a < \theta_b < 0, \\ 2\phi_{\max} - \theta_a - \theta_b, & 0 < \theta_b < 2\phi_{\max} - \theta_a, \\ 0, & 2\phi_{\max} - \theta_a < \theta_b < 2\phi_{\max}. \end{cases} \quad (16b)$$

In order to validate Eqs. (16), we apply Eq. (14) and recover the global density distribution in Eq. (10). Equations (16) are critical in determining the final triple-junction distribution, as they give the distribution of  $\theta_b$  for a given value of  $\theta_a$ . Once

the first two disorientations are assigned, the third is given explicitly by Eq. (6), and its density distribution is  $f(\theta_c) = f(-\theta_a - \theta_b)$ . The net distributions  $F(\theta)$  are obtained from the locally constrained ones  $f(\theta)$  using Eq. (14).

With the local density distributions determined at a given triple junction, we now need to identify what fraction of them will be classified as low-angle boundaries and derive the global coordination among such boundaries. To this end, we now divide the global distributions  $F(\theta)$  into several complementary distributions  $F_x^y$  in which  $y$  boundaries have been previously assigned,  $x$  of which were assigned a low-angle classification. This is merely a convenient separation of the subdistributions of different low- and high-angle coordinations, and the full distribution can be easily recovered from

$$\sum_{x=0}^y F_x^y(\theta) = F(\theta) \quad (17)$$

for any given value of  $y$  ( $= 0, 1$ , or  $2$ ). There are six functions  $F_x^y$  (where  $y$  ranges from  $0$  to  $2$  and  $x$  ranges from  $0$  to  $y$ ) which we omit here for the sake of brevity, but which are all readily derived in closed form through the use of Eqs. (14) and (16). Then the local transition probabilities  $\Pi_x^y$  can be found with the same construction that was used in determining the global low-angle fraction:

$$\Pi_x^y = \frac{\int_{-\theta_t}^{\theta_t} F_x^y(\theta) d\theta}{\int_{-2\phi_{\max}}^{2\phi_{\max}} F_x^y(\theta) d\theta}. \quad (18)$$

To clarify the method, consider the distribution  $F_0^0(\theta_a)$ , the distribution of  $\theta_a$  given no previously assigned boundaries; this distribution is given exactly by Eq. (10). Applying Eq. (18) to Eq. (10),  $\Pi_0^0$  is found to equal  $p$ . Evaluation of Eq. (18) for all possible triple-junction coordinations yields the following analytical expressions for  $\Pi_x^y$  in terms of  $q = 1 - p$ :

$$\Pi_0^0 = 1 - q, \quad (19a)$$

$$\Pi_0^1 = \begin{cases} \frac{1 - 6q^{1/2} + 15q - 10q^{3/2}}{3q}, & p < 0.75, \\ \frac{3 - 2q^{1/2}}{3}, & p > 0.75, \end{cases} \quad (19b)$$

$$\Pi_1^1 = \begin{cases} \frac{2 + 8q^{1/2} - 10q}{3 + 3q^{1/2}}, & p < 0.75, \\ \frac{3 - 6q + 2q^{3/2}}{3 - 3q}, & p > 0.75, \end{cases} \quad (19c)$$

$$\Pi_0^2 = \begin{cases} \frac{2 - 12q^{1/2} + 24q - 14q^{3/2}}{-1 + 6q^{1/2} - 12q + 10q^{3/2}}, & p < 0.75, \\ 1, & p > 0.75, \end{cases} \quad (19d)$$

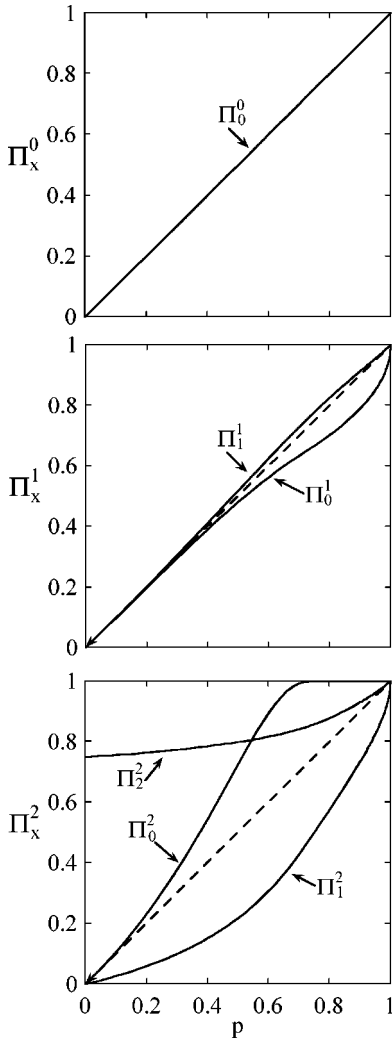


FIG. 9. Local transition probabilities  $\Pi_x^y$ , for  $y=0$  (a),  $y=1$  (b), and  $y=2$  (c), which give the local probability of assigning the next boundary as a low-angle boundary. The expectation value for a random lattice is given by the dashed line,  $\Pi_x^y=p$ . Deviations above this line indicate that a low-angle boundary is more likely to coordinate the junction, while deviations below indicate a lower probability.

$$\Pi_1^2 = \begin{cases} \frac{1-5q^{1/2}+4q}{-1+5q^{1/2}-10q}, & p < 0.75, \\ \frac{3-4q^{1/2}}{3-2q^{1/2}}, & p > 0.75, \end{cases} \quad (19e)$$

$$\Pi_2^2 = \begin{cases} \frac{3+6q^{1/2}}{2+10q^{1/2}}, & p < 0.75, \\ \frac{3-9q+6q^{3/2}}{3-6q+2q^{3/2}}, & p > 0.75. \end{cases} \quad (19f)$$

These functions are plotted in Fig. 9 for all values of the low-angle fraction. For a randomly assembled grain boundary network, each function  $\Pi_x^y$  would equal  $p$ , which is shown as a dashed line in Fig. 9. In these graphs, it is clear that only the first boundary may be assigned randomly;  $\Pi_0^0$  is

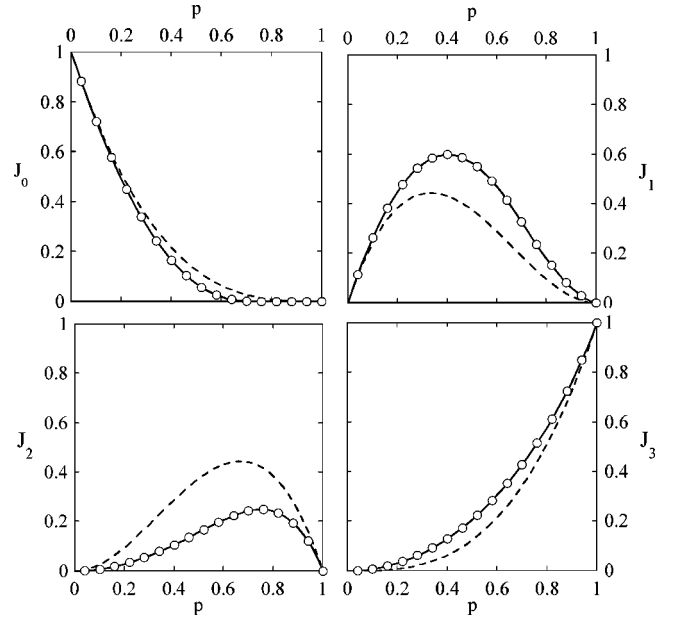


FIG. 10. Analytical triple-junction distribution for fiber-textured microstructure given by Eqs. (4) and (19) (solid line). Also shown are the simulated fiber-textured microstructures (points) and the distribution for a random lattice as given by Eq. (2) (dashed lines).

exactly equal to  $p$ . Deviations of  $\Pi_x^y$  from  $p$  indicate that the crystallographic constraint creates triple junctions with low-angle boundaries more (or less) frequently than expected. Where any of the curves  $\Pi_x^y$  lies above  $p$ , it is more likely for a low-angle boundary to coordinate the junction, while if it falls below  $p$ , a high-angle boundary is more likely.

As the number of previously assigned boundaries increases from 0 to 2, the constraint on the system increases, as Eq. (6) must be strictly obeyed. For example, the distributions  $\Pi_x^1$  are only weakly constrained by the assignment of the first boundary; in Fig. 9(b),  $\Pi_0^1$  and  $\Pi_1^1$  deviate only slightly from  $p$ . While the range of  $\theta_b$  is limited for any specific  $\theta_a$  [Eq. (6)], there is only a small effect when integrated over all values of  $\theta_a$ . If the first boundary ( $a$ ) is a high-angle boundary, the density distribution of the second boundary ( $b$ ) is weighted such that boundaries with high disorientation angles are more probable [i.e.,  $\Pi_0^1 < p$  in Fig. 9(b).] Similarly, if the first boundary is a low-angle boundary, there is a slight tendency for another low-angle boundary to coordinate the junction [i.e.,  $\Pi_1^1 > p$  in Fig. 9(b)]. In both cases the density distribution of the second boundary is *not* random, but its deviation from  $\Pi_x^1=p$  is rather small.

The most dominant effects of the crystallographic constraint appear after two boundaries have been previously assigned. Unlike when only  $\theta_a$  had been assigned and  $\theta_b$  was still relatively free, the assignment of  $\theta_a$  and  $\theta_b$  necessarily fixes  $\theta_c$  [Eq. (6)]. Therefore, for a given  $\theta_a$  and  $\theta_b$ , there will be only one  $\theta_c$  allowed, representing a much stricter constraint on possible triple-junction combinations. This is seen as the density distribution functions  $\Pi_x^2$  [Fig. 9(c)] deviate significantly from the random case.

With the expressions for  $\Pi_x^y$  in hand, a full closed-form solution for the triple-junction distribution is obtained by in-

roducing them into Eq. (4). In Fig. 10, this solution for  $J_i$  is shown by the solid lines, while the data points are the results of computer simulations. Shown for comparison as dashed lines are the random distributions of Eqs. (2). Clearly, the analytical model and computer simulations give identical results, distinctly different from the purely probabilistic approach. To our knowledge, this is the first closed-form analytical solution for the triple-junction distribution of a polycrystal.

The analytical derivation of  $\Pi_x^y$  also gives significant insight into the crystallographic constraints in polycrystals, especially with regard to the assignment of the third boundary  $\Pi_x^2$ .

(i) In Fig. 9(c), for all values of the low-angle fraction,  $\Pi_0^2$  is greater than  $p$ , such that if two high-angle boundaries coordinate a junction, it is likely that the third boundary will be a low-angle boundary. This is manifested in the triple-junction distribution (Fig. 10) by an increase in  $J_1$  junctions and a reduction in  $J_0$  junctions. When  $p \geq 0.75$  ( $\theta_i \geq \phi_{\max}$ ),  $\Pi_0^2 = 1$  and there cannot be any  $J_0$  junctions (two high-angle boundaries will always result in a low-angle boundary). Since boundaries  $a$  and  $b$  have been assigned as high-angle boundaries,  $\theta_c$  must be less than  $\phi_{\max}$  (and therefore  $\theta_i$ ) according to Eq. (6).

(ii) For all values of  $p$ ,  $\Pi_1^2$  is lower than the expected random value, meaning that at junctions coordinated by one low- and one high-angle boundary, the third boundary will frequently be a high-angle boundary. This constraint increases the population of  $J_1$  junctions further, while decreasing the population of  $J_2$  junctions.

(iii) The deviation of  $\Pi_2^2$  above the line  $\Pi_x^y = p$  contributes more strongly to the decreased population of  $J_2$  junctions

in the networks. The presence of two low-angle boundaries strongly promotes the presence of a third, so that  $J_2$  junctions are produced infrequently while  $J_3$  junctions are profuse.

## V. CONCLUSIONS

Standard percolation theory, in which bonds are randomly assigned as “strong” or “weak” links, has been shown to be insufficient for modeling networks of low- and high-angle interfaces in polycrystals. Both 2D computer simulations and a new assessment of existing experimental data have revealed a nonrandom distribution of triple-junction types, an indication that topological correlations are present. We have shown how this nonrandom behavior is due to local crystallographic constraints at triple junctions and identified the corresponding shifts in the percolation thresholds. An analytical model was developed for fiber-textured microstructures and a closed-form analytical expression for the triple-junction distribution derived. By identifying local transition probabilities for the assignment of low-angle boundaries at a triple junction, we obtain new insight into the nature of the crystallographic constraint.

## ACKNOWLEDGMENTS

This work was supported by both the Chemistry and Materials Sciences Directorate of Lawrence Livermore National Laboratory and the National Science Foundation under Contract No. DMR-0346848 although the views expressed here are not endorsed by the sponsors.

- 
- <sup>1</sup>L. C. Lim and T. Watanabe, *Acta Metall. Mater.* **38**, 2507 (1990).  
<sup>2</sup>T. Watanabe, *Mater. Sci. Eng., A* **176**, 39 (1994).  
<sup>3</sup>K. T. Aust, U. Erb, and G. Palumbo, *Mater. Sci. Eng., A* **176**, 329 (1994).  
<sup>4</sup>G. Palumbo, P. J. King, K. T. Aust, U. Erb, and P. C. Lichtenberger, *Scr. Metall. Mater.* **25**, 1775 (1991).  
<sup>5</sup>M. A. Gaudett and J. R. Scully, *Metall. Mater. Trans. A* **25**, 775 (1994).  
<sup>6</sup>V. Y. Gertsman and K. Tangri, *Acta Mater.* **45**, 4107 (1997).  
<sup>7</sup>G. Wang, L. Zuo, and C. Esling, *Philos. Mag. A* **82**, 2499 (2002).  
<sup>8</sup>D. B. Wells, J. Stewart, A. W. Herbert, P. M. Scott, and D. E. Williams, *Corrosion (Houston)* **45**, 649 (1989).  
<sup>9</sup>E. M. Lehigh, G. Palumbo, P. Lin, and A. Brennenstuhl, *Metall. Mater. Trans. A* **29**, 387 (1998).  
<sup>10</sup>J. H. Park and B. T. Ahn, *J. Appl. Phys.* **93**, 883 (2003).  
<sup>11</sup>O. V. Kononenko, V. N. Matveev, and D. P. Field, *J. Mater. Res.* **16**, 2124 (2001).  
<sup>12</sup>J. A. Pfaendtner and C. J. McMahon, Jr., *Acta Mater.* **49**, 3369 (2001).  
<sup>13</sup>R. C. Muthiah, J. A. Pfaendtner, S. Ishikawa, and C. J. McMahon, Jr., *Acta Mater.* **47**, 2797 (1999).  
<sup>14</sup>V. Traskine, P. Protsenko, Z. Skvortsova, and P. Volovitch, *Colloids Surf., A* **166**, 261 (2000).  
<sup>15</sup>R. Le Gall and G. Saindrenan, *Interface Sci.* **11**, 59 (2003).  
<sup>16</sup>H. E. Roman, A. Bunde, and W. Dieterich, *Phys. Rev. B* **34**, 3439 (1986).  
<sup>17</sup>L. Martin-Carron, R. Ramirez, C. Prieto, A. de Andres, J. Sanchez-Benitez, M. Garcia-Hernandez, and J. L. Martinez, *J. Alloys Compd.* **323–324**, 527 (2001).  
<sup>18</sup>T. Terashige and K. Okano, *IEEE Trans. Electron Devices* **46**, 555 (1999).  
<sup>19</sup>B. Zeimetz, B. A. Glowacki, and J. E. Evetts, *Physica C* **372–376**, 767 (2002).  
<sup>20</sup>B. Zeimetz, B. A. Glowacki, and J. E. Evetts, *Eur. Phys. J. B* **29**, 359 (2002).  
<sup>21</sup>N. A. Rutter, B. A. Glowacki, and J. E. Evetts, *Supercond. Sci. Technol.* **13**, L25 (2000).  
<sup>22</sup>E. D. Specht, A. Goyal, and D. M. Kroeger, *Supercond. Sci. Technol.* **13**, 592 (2000).  
<sup>23</sup>Z. X. Cai and D. O. Welch, *Phys. Rev. B* **45**, 2385 (1992).  
<sup>24</sup>A. S. Argon and Y. Qiao, *Philos. Mag. A* **82**, 3333 (2002).  
<sup>25</sup>Y. Qiao and A. S. Argon, *Mech. Mater.* **35**, 129 (2003).  
<sup>26</sup>Y. Qiao and A. S. Argon, *Mech. Mater.* **35**, 313 (2003).  
<sup>27</sup>S. Ju, H. Sun, and Z.-Y. Li, *J. Phys.: Condens. Matter* **14**, L631 (2002).

- <sup>28</sup>D. Stauffer and A. Aharony, *Introduction to Percolation Theory* (Taylor & Francis, London, 1992).
- <sup>29</sup>V. Y. Gertsman and K. Tangri, *Scr. Metall. Mater.* **32**, 1649 (1995).
- <sup>30</sup>J.-Q. Su, M. Demura, and T. Hirano, *Acta Mater.* **51**, 2505 (2003).
- <sup>31</sup>G. Winther, *Acta Mater.* **51**, 417 (2003).
- <sup>32</sup>T. C. Lee, I. M. Robertson, and H. K. Birnbaum, *Philos. Mag. A* **62**, 131 (1990).
- <sup>33</sup>D. G. Brandon, *Acta Metall.* **14**, 1479 (1966).
- <sup>34</sup>M. Dechamps, F. Baribier, and A. Marrouche, *Acta Metall.* **35**, 101 (1987).
- <sup>35</sup>G. Palumbo, K. T. Aust, E. M. Lehockey, U. Erb, and P. Lin, *Scr. Mater.* **38**, 1685 (1998).
- <sup>36</sup>C. A. Schuh, M. Kumar, and W. E. King, *Acta Mater.* **51**, 687 (2003).
- <sup>37</sup>M. Kumar, W. E. King, and A. J. Schwartz, *Acta Mater.* **48**, 2081 (2000).
- <sup>38</sup>C. A. Schuh, R. W. Minich, and M. Kumar, *Philos. Mag. A* **83**, 711 (2003).
- <sup>39</sup>M. Frary and C. A. Schuh, *Appl. Phys. Lett.* **83**, 3755 (2003).
- <sup>40</sup>V. Y. Gertsman and K. Tangri, *Acta Metall. Mater.* **43**, 2317 (1995).
- <sup>41</sup>P. Davies, V. Randle, G. Watkins, and H. Davies, *J. Mater. Sci.* **37**, 4203 (2002).
- <sup>42</sup>R. W. Minich, C. A. Schuh, and M. Kumar, *Phys. Rev. B* **66**, 052101 (2002).
- <sup>43</sup>P. Fortier, W. A. Miller, and K. T. Aust, *Acta Mater.* **45**, 3459 (1997).
- <sup>44</sup>D. J. Dingley and V. Randle, *J. Mater. Sci.* **27**, 4545 (1992).
- <sup>45</sup>J. Furley and V. Randle, *Mater. Sci. Technol.* **7**, 12 (1991).
- <sup>46</sup>V. Randle, *Acta Metall. Mater.* **43**, 1741 (1995).
- <sup>47</sup>A. Goyal, E. D. Specht, D. M. Kroeger, T. A. Mason, D. J. Dingley, G. N. Riley, and M. W. Rupich, *Appl. Phys. Lett.* **66**, 2903 (1995).
- <sup>48</sup>J. Bystrzycki, R. A. Varin, M. Nowell, and K. J. Kurzydowski, *Intermetallics* **8**, 1049 (2000).
- <sup>49</sup>D. Weiss, O. Kraft, and E. Arzt, *J. Mater. Res.* **17**, 1363 (2002).
- <sup>50</sup>D. M. Feldmann, J. L. Reeves, A. A. Polyanskii, G. Kozlowski, R. R. Biggers, R. M. Nekkanti, I. Maartense, M. Tomsic, P. Barnes, C. E. Oberly, T. L. Peterson, S. E. Babcock, and D. C. Larbalestier, *Appl. Phys. Lett.* **77**, 2906 (2000).
- <sup>51</sup>J. Liu and J. G. Morris, *Metall. Mater. Trans. A* **34**, 951 (2003).
- <sup>52</sup>V. Randle, *Acta Metall. Mater.* **42**, 1769 (1994).
- <sup>53</sup>A. Goyal, E. D. Specht, Z. L. Wang, and D. M. Kroeger, *Ultra-microscopy* **67**, 35 (1997).
- <sup>54</sup>L. Fernandez, B. Holzappel, F. Schindler, B. deBoer, A. Attenberger, J. Hanisch, and L. Schultz, *Phys. Rev. B* **67**, 052503 (2003).
- <sup>55</sup>Y. Iijima, K. Onabe, N. Futaki, N. Tanabe, N. Sadakata, O. Kohno, and Y. Ikeno, *J. Appl. Phys.* **74**, 1905 (1993).
- <sup>56</sup>A. Goyal, D. P. Norton, D. M. Kroeger, D. K. Christen, M. Paranthaman, E. D. Specht, J. D. Budai, Q. He, B. Saffian, F. A. List, D. F. Lee, E. Hartfield, P. M. Martin, C. E. Klabunde, J. Mathis, and C. Park, *J. Mater. Res.* **12**, 2924 (1997).
- <sup>57</sup>D. J. Dingley, in *Electron Backscatter Diffraction in Materials Science*, edited by B. L. Adams (Kluwer Academic, New York, 2000), p. 1.
- <sup>58</sup>U. F. Kocks, C. N. Tome, and H.-R. Wenk, *Texture and Anisotropy* (Cambridge University Press, Cambridge, UK, 1998).
- <sup>59</sup>J. Hoshen and R. Kopelman, *Phys. Rev. B* **14**, 3438 (1976).
- <sup>60</sup>J. K. MacKenzie, *Biometrika* **45**, 229 (1958).
- <sup>61</sup>A. Morawiec, *J. Appl. Crystallogr.* **28**, 289 (1995).
- <sup>62</sup>H. S. Ryoo, S. K. Hwang, M. H. Kim, S. I. Kwun, and S. W. Chae, *Scr. Mater.* **44**, 2583 (2001).
- <sup>63</sup>V. Randle, *Modell. Simul. Mater. Sci. Eng.* **4**, 455 (1996).
- <sup>64</sup>A. Garbacz and M. W. Grabski, *Acta Metall. Mater.* **41**, 475 (1993).
- <sup>65</sup>M. Frary and C. A. Schuh, *Acta Mater.* **51**, 3731 (2003).